

ARTICLE OPEN

Inkjet-printed MXene micro-scale devices for integrated broadband ultrafast photonics

Xiantao Jiang^{1,2,5}, Wenjia Li², Ting Hai³, Rui Yue², Zhangwei Chen⁴, Changshi Lao⁴, Yanqi Ge^{1,2}, Guoqiang Xie³, Qiao Wen^{1b} and Han Zhang^{1,2}

MXene, as a novel 2D crystal material, possessing tunable bandgap, low optical attenuation and broadband nonlinear optical responses that may promote the fabrications of advanced electro-photonics devices has gathered remarkable attention recently. However, current investigations of 2D crystals for photonics devices suffer from the limitations of reproducibility, scalability, and compatibility. Inkjet printing is one of the powerful additive manufacturers that facilitate well-controlled, low-cost, scalable and small-footprint electro-photonics devices on myriad substrates. Herein, we directly inkjet printed MXene nanosheets in laser resonators with both fiber and free-space geometrics, and achieved extensive spectral band ultrafast laser operations from near- to the mid-infrared regime with pulse duration going to 100 femtoseconds. The demonstrations of versatile inkjet-printed devices based on MXene, while forthputting its distinct electro-optical properties, may allow the realizations of advanced MXene enable photonics devices shortly.

npj 2D Materials and Applications (2019)3:34; <https://doi.org/10.1038/s41699-019-0117-3>

MXene,¹ as a glaring multi-feature two-dimensional (2D) crystal, has recently experienced a rapid proliferation of interests from energy storage,² medical therapy³, and imaging,⁴ electromagnetic interference (EMI) shielding,⁵ catalyst,⁶ sea water purification,⁷ ultrafast photonics,⁸ to only name a few. MXene represents a big family with the chemical composition of $M_{n+1}X_nT_x$, where M is an early transition metal, X is C and/or N, T is the surface terminations (–OH, –O or –F), and $n = 1, 2$, or 3 . The chemical richness and 2D atomical layer structure of MXene equip themselves with variable and tailorable physical and chemical properties. Specifically, the large bandgap tunability,^{9–14} a suggested lower optical attenuation^{15,16} compared to the well-known graphene 2.3% per atomical layer,¹⁷ and the broadband (0.8–1.8 μm) nonlinear optical responses⁸ of MXene indicate the huge potential to be taken for efficiently light manipulations. However, there have been only a few attempts to utilize the excellent optical properties for plasmonics¹⁸ and ultrashort laser generations from 1.06 to 1.88 μm ^{8,19–21} through drop cast or spin-coating. Yet, these techniques suffer from the bottlenecks of reproducibility, scalability, and compatibility. MXenes can be available either via top-down acid etching method¹ or through bottom-up CVD approach.²² The previous one overwhelming the other approaches in the aspects of feasibility, yielding, controllability and finance efficiency. Thus, the fine-controlled solution processed techniques are reckoned as the primary way to utilize MXene for device fabrications.

Inkjet printing is a forefront technique to exploit the merits of 2D materials for printed optoelectronic devices with small-footprint, integration, substrates/geometrics compatibility, scalability, and low cost. Indeed, a large variety of 2D materials, including reduced

graphene oxide,^{23–28} graphene,^{29–42} transition metal dichalcogenides,^{31,34,38,39,42,43} boron nitride,^{31,34,40–42} as well as black phosphorus⁴⁴ have been incorporated into the printing inks to construct electrodes, photodetectors, gas/strain sensors, transistors, supercapacitors, photovoltaic devices, read-only memories, EMI shield and so forth. Success inkjet-printed pattern realization is the interplay result of substrates, ink rheological properties and printer parameters.^{45,46} The choosing of ink solutions is regarded as the key point. High viscosity solution like N-methyl-2-pyrrolidone (NMP) and dimethyl sulfoxide (DMSO) are normally used in the 2D material liquid exfoliation processes, and thus can be directly used for ink formulation. However, high-temperature annealing after-treatment may be incurred to remove the polymers which will impair the performance of 2D crystals.^{29,31,38–40} Single or mixed low boiling point alcohols (e.g., ethanol, 2-butanol, isopropanol) and biological compatible water are also proposed as the ink solutions with careful ink surface tension and viscosity engineering.^{23,30–34,37,41,42} A small amount of polymers or proteins can also be added into the solutions that act as “binders” to improve the printed film uniformity. Very recently, the viable of printed MXene has been demonstrated with a DMSO + protein formulated ink, where a large diameter nozzle (125 μm) is required, and thus the spatial pattern resolution is limited to 120 μm .⁴⁷

In this paper, metallic titanium carbide $\text{Ti}_3\text{C}_2\text{T}_x$ MXene is deliberately chosen and prepared via acid etching approach. Low boiling point, non-toxic, “binder-free” MXene nanosheets ink is formulated using isopropanol (IPA, boiling point 82.6 °C) for establishing functional devices on silica glass, SiO_2/Si wafer, side-polished fiber, flexible and transparent PET film, and gold mirror

¹Shenzhen Engineering Laboratory of Phosphorene and Optoelectronics, Collaborative Innovation Center for Optoelectronic Science and Technology, College of Optoelectronic Engineering, Shenzhen University, Shenzhen 518060, China; ²Key Laboratory of Optoelectronic Devices and Systems of Ministry of Education and Guangdong Province, College of Optoelectronic Engineering, Shenzhen University, Shenzhen 518060, China; ³Key Laboratory Laser Plasmas, Collaborative Innovation center of IFSA (CICIFSA), School of Physics and Astronomy, Shanghai Jiao Tong University, Shanghai 200240, China; ⁴Additive Manufacturing Institute, College of Mechatronics and Control Engineering, Shenzhen University, Shenzhen 518060, China and ⁵College of Chemistry and Environmental Engineering, Shenzhen University, Shenzhen 518060, China

Correspondence: Guoqiang Xie (xieqg@sjtu.edu.cn) or Qiao Wen (wenqiao@szu.edu.cn) or Han Zhang (hzhang@szu.edu.cn)

These authors contributed equally: Xiantao Jiang, Wenjia Li

Received: 27 March 2019 Accepted: 26 July 2019

Published online: 04 September 2019

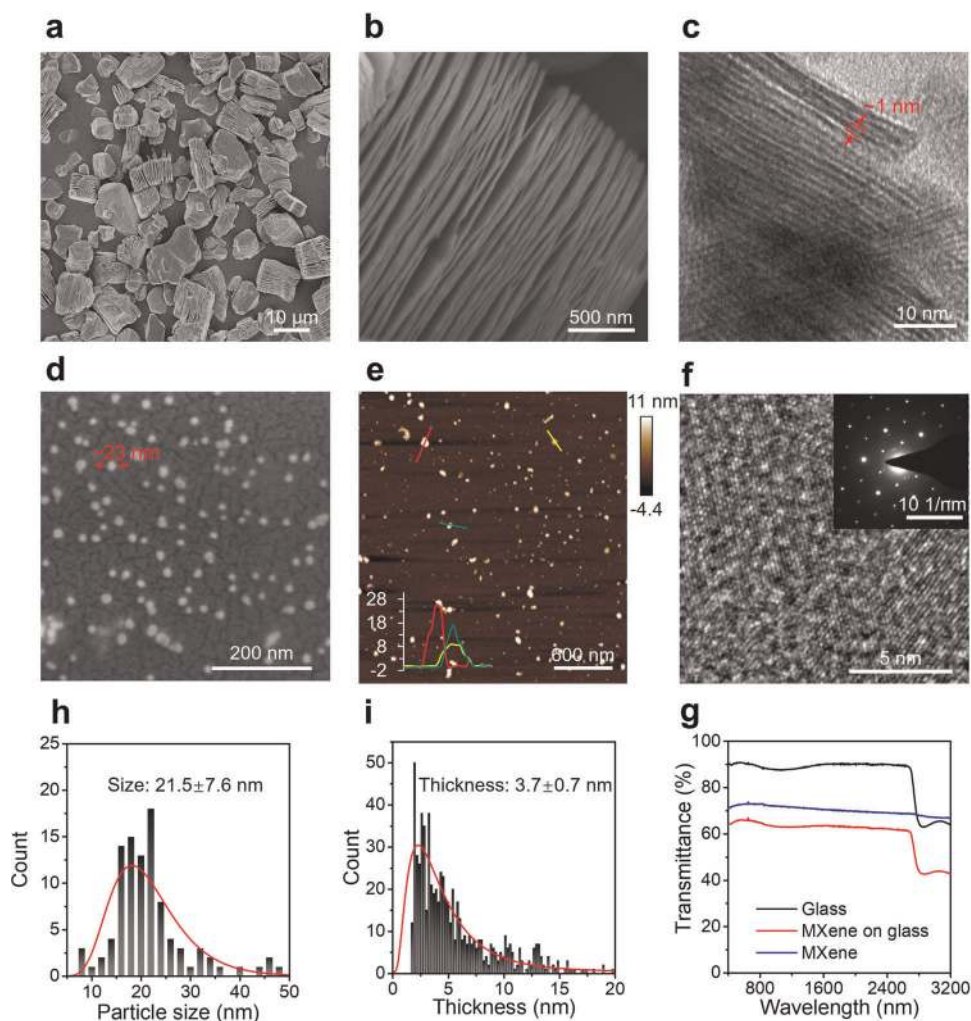


Fig. 1 Morphological characterizations of MXene. **a** SEM image of the prepared MXene powder via acid etching technique. **b** The zoom-in SEM image of MXene. **c** HRTEM image shows the interlayer thickness of MXene. **d** SEM and **e** AFM image of the MXene nanosheets in the IPA ink precursor. **f** HRTEM image of MXene nanosheets; inset: the corresponding SEAD pattern. **h** Size (Feret's diameter) and **i** thickness distributions of the nanosheets characterized via SEM and AFM, respectively. **g** The optical transmission of MXene nanosheets deposited on a silica glass substrate

substrates. To advance the utilize of the broadband nonlinear optical responses of MXene, the printed side-polished fiber and gold mirror have been integrated to both fiber and solid-state laser resonators, to achieve ultrafast laser operations covering the optical spectrum of 1–3 μm . Mode-locking operation with pulse duration going to 100 fs has been achieved at the telecommunication window, while Q-switched lasers have been demonstrated in solid-state resonators and in the mid-infrared regime. The virtue of the demonstrations not only lies on broadband ultrafast laser generations via versatile printed MXene photonic devices but are also anticipated to point out a methodology for complex laser resonators integration with functional 2D crystal materials.

RESULTS AND DISCUSSION

Ink formulation

In this contribution, titanium carbide ($\text{Ti}_3\text{C}_2\text{T}_x$) MXene was prepared via feasible acid etching method, as described in Ref. ⁸. The delaminated $\text{Ti}_3\text{C}_2\text{T}_x$ was then washed by de-ionic water and dried. The morphology of the prepared MXene is shown in Fig. 1a, b, where typical accordion-like structures can be clarified, confirms the good extraction of Al atoms from its corresponding MAX phase Ti_3AlC_2 . The atomic lattice was characterized to be

hexagonal space group $\text{P6}_3/\text{mmc}$ (Fig. 1f) with an interlayer distance of ~ 1 nm (Fig. 1c), which is in agreement with the theoretical predictions.⁴⁸ The particle size of the obtained MXene powder after acid etching procedures is around 10–30 μm (see Fig. 1a), which can result in nozzle clogging during the inkjet printing. Typically, the particle size should be smaller than 1/50 the of the nozzle diameter in order to avoid nozzle choking.^{29,49} Therefore, the MXene particle size is required to be smaller than 400 nm when using a 22 μm nozzle. To reduce the particle size, the prepared MXene powder was firstly dispersed into isopropyl alcohol (IPA) solution with a concentration of 5 mg/ml and then underwent violent ultrasonic bath in ice-cooled water over 72 h. After this, a home-made vacuum filtration apparatus with a polytetrafluoroethylene (PTFE) membrane (pore size ~ 220 nm) was used to separate the produced MXene nanosheets into a flask. The mean particle size (Feret's diameter) and thickness of the MXene nanosheets in the IPA solution were checked via SEM and AFM to be 21.5 ± 7.6 nm and 3.7 ± 0.7 nm, respectively, well satisfy the particle size requirements of printing (see Fig. 1d, e). However, we found the concentration of MXene nanosheets is rather low after separation for efficiently pattern fulfillment, even though multiple passes are applied. The MXene nanosheets IPA solution was then concentrated via a rotavapor to formulate the ink. The

concentration of the MXene ink was characterized to be ~ 2 mg/ml. Previously, efficient inkjet-printed devices have been reported using an ink concentration as low as tens $\mu\text{g/ml}$ in different solutions,³¹ indicating that the concentration of the materials is not a stringent prerequisite. However, a higher ink concentration features synergistic advantages to the final productions, such as reduces the printing time, higher uniformity due to the material pinning effect that effectively avoids the material carry during the ink drying, alleviates the re-dispersion. The optical attenuation of MXene ink drop cast on a silica glass is presented in Fig. 1g, which shows an impartial absorption from 400 to 3000 nm, agrees well with its zero bandgap (or $E_g < 0.2$ eV) electronic band structure,¹ and indicating the broadband nonlinear optical modulation spectral window.

The devices pattern is constructed via the deposition of multiple single ink droplets that determine the print pixel resolution, thus, the engineering of the single droplet is of crucial for the device fabrications. Stable ejecting of single droplets from a given nozzle can be qualitatively estimated by the inverse Ohnesorge number $Z = \frac{\sqrt{\rho\gamma d}}{\eta}$, where ρ , γ , and η represents the ink density, surface tension and viscosity respectively, d is the diameter of the nozzle. An unitless value of Z between 1 and 14 suggests a stable single droplet ejecting. Ink with Z value smaller than 1 is hard to be ejected, while with Z larger than 14 tend to generate satellite droplets.^{46,50} A brief summary of rheological properties of the formulated 2D materials ink is presented in Table 1. The obtained MXene ink features a density of 0.79 g/cm^3 , surface tension of 23 mN/m , viscosity of 2.4 mPas , thus giving $Z \sim 8.3$, which is similar to recently reported ink based on black phosphorus⁴⁴ and h-boron nitride.⁴⁰ The prepared MXene nanosheets ink can stable for more than three months in a fridge, without particle aggregation and ink stratification were observed. This might be due to the high negative zeta potential of MXene nanosheets.⁵¹ A stable ejected droplet sequences observed from the printer stroboscopic camera is presented in Fig. 2b. The droplet is further required to wet the substrate to form a continuous coating though the ink is suitable for stable ejecting.⁴⁵ Previous reports suggest the ink surface tension should be $7\text{--}10 \text{ mN/m}$ lower than the substrate surface energy.⁴⁴ The as-prepared MXene ink is suitable for substrates including silicate glass, SiO_2/Si wafer ($\text{SiO}_2 \sim 36 \text{ mN/m}$ ⁵²), and polyethylene terephthalate (PET, $\sim 48 \text{ mN/m}$ ⁵³). All of them have been applied without any surface treatments in this project to confirm the ink's wide adaptability.

After printing, the droplet drying process is another key point for the final device quality. The higher evaporation ratio at the outer edge of the droplets could lead to the outward capillary flows that carry the material to the external edge and create the well-known non-uniform "coffee ring" effect. To avoid the "coffee ring" effect, several strategies have been proposed, including mixed solutions with different surface tensions to form the reverse Marangoni flows, low surface tension to achieve high-level wetting, large particle size, high ink concentration or polymer/protein binders to "freeze" the particles, low solution evaporation temperature to mediate the evaporation ratio difference, to demonstrate well-printed functional devices.^{30,35,54,55} Herein, IPA with low surface tension and low evaporation temperature (82.6°C) was chosen as the ink solution, and the dispersed MXene nanosheets in that IPA solution was concentrated to alleviate the printed pattern non-uniformity. Through these means, negligible "coffee ring" can be observed experimentally on both the substrates (see Fig. 2 and Supplementary Information).

Device fabrications

The ability of inkjet printing to form arbitrary 2D or quasi-3D patterns via the deposition of single ink droplets has significantly

promoted the explorations of advanced micro electro-optical devices based on two-dimensional crystals.^{31,37,39,40,42} Previous studies indicate that MXene can be a promising broadband saturable absorber from visible to the mid-infrared regime with linear optical losses as low as $\sim 1\%/ \text{nm}$.^{8,16,19} However, the integration to the laser resonators and the finely controlled deposition thickness, geometrics, and dimensions remain been barely touched to date. Hence, we adopted a side-polished fiber and a gold mirror as the substrates to form the saturable absorber devices in pursuit of integration with different laser resonator setups. In the printing process (DMP-2850, FUJIFILM Dimatix), the substrate temperature is 50°C , the voltage for the nozzle actuator is $18\text{--}23 \text{ mV}$ depends on the nozzle chosen, the tickle frequency is 23 kHz . By altering the inter-droplet distance, different patterns such as dots matrix, stripes and be printed as required (see Fig. 2d, e). Decreasing the inter-droplet distance to $35 \mu\text{m}$, uniform and continuous MXene nanosheets film can be obtained on the substrates. We found multi-passes could help to improve the film uniformity due to the small inter-droplet distance. A range of printed layers on both side-polished fiber (4 L, 6 L, 8 L, 10 L, 12 L; L: layer) and gold mirror (4 L, 8 L, 10 L, 16 L, 20 L) samples were prepared to engineer the saturable absorption properties for particular resonators. There are a 5 min break every two passes for drying on the side-polished fiber (as well as glass, PET, SiO_2/Si wafer), while for the thicker gold mirror substrate, the drying time could last about more than 10 min at 60°C . Subtle stacking trace and white light interference colors can be recognized from Fig. 2f, k. Note, the printing technique can be agilely transformed on the substrates of glass, transparent and flexible PET film, silica/silicon wafer for specified applications (see Supplementary Information). Figure 2c shows a logo of "Shenzhen University" that been printed on a transparent and flexible PET film via using the MXene nanosheets ink.

Laser performance

The investigation of ultrafast lasers with high electric field amplitude, short temporal duration and high repetition rate, driven by the wide application demands in both civil and military industries has found fruitful achievements via semiconductor saturable absorber mirror (SESAM).⁵⁶ However, the sophisticated fabrication processes and the limited frequency bandwidth of SESAM encounters the barriers of high financial cost, low compatibility, and narrow modulation bandwidth. Alternatives based on low dimensional materials, such as graphene, carbon nanotubes (CNTs), topological insulators, transition metal dichalcogenides, and epsilon-near-zero (ENZ) medium have recently been proposed,^{57,58} with which broadband optical modulation capability, low optical loss, high modulation depth and low bleaching threshold have been demonstrated. Even though, the exploiting of broadband saturable absorbers, especially for the mid-infrared laser sources based on low-dimensional materials is far for closure, in the aspects of fabrication technologies, materials, resonator geometrics, and optical mechanisms.

To demonstrate the broadband optical amplitude modulations and wide adaptability of the printed MXene saturable absorbers, four laser resonators with different operating wavelengths and configurations were designed and established. Figure 3a, b shows the architecture of all-fiber ring resonators with ytterbium- and erbium-doped fiber as the gain medium. The length of the Yb-doped (250 dB/m @ 980 nm , $8/125 \mu\text{m}$) and Er-doped (4.45 dB/m @ 980 nm , $8/125 \mu\text{m}$) fiber are 1 and 4 meters, results in cavity length of 12.7 and 17.8 meters, respectively. The ring oscillator consists of a laser diode (LD, 980 nm , $P_{\text{max}} = 700 \text{ mW}$) as the pump, a wavelength division multiplexer (WDM) for input coupling, the impurified gain medium, a polarization controller (PC), a polarization independent isolator (PI-ISO), an optical coupler (OC, 10%), and the side-polished fiber saturable absorber.

Table 1. A brief summary of inkjet-printed 2D materials rheological properties (Concentration C (mg/ml), density ρ (g/cm^3), surface tension γ (mN/m), viscosity η (mPas), nozzle diameter d (μm), inverse Ohnesorge number Z) and the applications

2D crystals	Ink solution recipes	Rheological properties	Devices and pixel resolution (r , μm)	Refs.
Graphene	Ethylene glycol + N-methyl-2-pyrrolidone	$C \sim 0.11$, $\rho = 1.05\text{--}1.08$, $\gamma = 42\text{--}46$, $\eta = 4.2\text{--}18$, $d = 50$, $Z = 2.8\text{--}11.2$	$r = 70\text{--}100$, Transistors	29
	Terpineol + ethanol + polymer	$C = 1$	Transistors, supercapacitors, $r \sim 60$	30
	N-methyl-2-pyrrolidone	$C = 0.01$, $Z = 23$	Transistors, photovoltaic devices	31
	Ethyl cellulose + cyclohexanone + terpineol	$C = 3.4$, $\gamma = 33$, $\eta = 11\text{mPas}$, $0.1\text{--}1$ kHz shear rate	Flexible electronic patterns, $r \sim 50$	32,33
	Polyvinylpyrrolidone + isopropanol	$C = 0.42$, $\rho = 0.8$, $\gamma = 28$, $\eta = 2.3$, $d = 22$, $Z = 9.6$	Humidity sensor, electrodes for solar cell	35,36
	Cyclohexanone + terpineol + ethyl cellulose	$C = 2.3$	Supercapacitors	37
	N-methyl-2-pyrrolidone	$C = 1.6$, $\rho \sim 1$, $\gamma = 33.7$, $\eta = 1.65$, $d = 21$, $Z \sim 17$	Transistors, capacitors	38–40
	Ethanol	$C = 0.42$, $\rho = 0.82$, $\gamma = 30$, $\eta = 1$, $d = 21$, $Z = 22$	Wearable and textile electronics	41
	Water + triton x-100 + propyleneglycol + xanthan gum	$C = 2$, $\rho \sim 1.1$, $\gamma = 40$, $\eta = 1.37$, $d = 21.5$, $Z \sim 20$	Photodetectors, read-only memories, $r = 60 \sim 80$	42
	Reduced graphene oxide	Water + polyethylene	$C = 3$ mg/ml $\rho \sim 1$	All-organic vapor sensor
MoS ₂	Water	$\rho \sim 1$, $\gamma = 72.8$, $\eta = 2.2$	Dipole-antenna, $r \sim 70$	24
	Water	$C = 5 \sim 9$	Electric circuits, chemical sensors	25
	Water	$C = 0.2$ wt%, $\rho \sim 1$, $\gamma = 68$, $\eta = 1.06$	Electrodes, $r \sim 50$	26
	Water	$\gamma = 75.2$	Acoustic actuators	27
	Water	$C = 2$	Electrodes, $r \sim 60$	67
	Terpineol + ethanol + ethyl cellulose	$C = 0.1$	Transistors, photodetectors, $r \sim 80$	43
	Ethanol + water	$C = 0.04$, $d = 23$	Transistors, photovoltaic devices	31
	N-methyl-2-pyrrolidone	$C \sim 1.6$, $\rho \sim 1$, $\gamma = 33.7$, $\eta = 1.65$, $d = 21$, $Z \sim 17$	Capacitors	38
	Water + triton x-100 + propyleneglycol + xanthan gum	$C = 2$, $\rho \sim 1.1$, $\gamma = 40$, $\eta = 1.37$, $d = 21.5$, $Z \sim 20$	Photodetectors, read-only memories, $r = 60 \sim 80$	42
	WS ₂	Ethanol + water	$C = 0.056$, $d = 23$	Transistors, photovoltaic devices
WSe ₂	Water + triton x-100 + propylene glycol + xanthan gum	$C = 2$, $\rho \sim 1.1$, $\gamma = 40$, $\eta = 1.37$, $d = 21.5$, $Z \sim 20$	Photodetectors, read-only memories, $r = 60 \sim 80$	42
	N-methyl-2-pyrrolidone	$C = 1.5$, $\rho \sim 1$, $\gamma = 33.7$, $\eta = 1.65$, $d = 21$, $Z \sim 17$	Transistors	39
	Water + Py-1SO ₃	$C = 0.104$, $d = 23$	Transistors, photovoltaic devices	31
	Isopropanol	$C = 0.5$, $\rho \sim 0.79$, $\gamma = 23$, $\eta = 2.4$, $d = 21$, $Z \sim 8.3$	Capacitors	40
	Water + carboxymethylcellulose sodium salt	$C = 0.44$, $\rho = 1.01$, $\gamma = 72$, $\eta = 1.7$, $d = 21$, $Z = 19.4$	Wearable and textile electronics	41
	Water + triton x-100 + propylene glycol + xanthan gum	$C = 2$, $\rho \sim 1.1$, $\gamma = 40$, $\eta = 1.37$, $d = 21.5$, $Z \sim 20$	Photodetectors, read-only memories, $r = 60 \sim 80$	42
	Isopropanol + 2-butanol	$C = 5$, $\rho \sim 0.8$, $\gamma = 28$, $\eta = 2.2$, $d = 22$, $Z \sim 10$	Fiber ML laser, photodetectors, $r = 60 \sim 80$	44
	Dimethyl sulfoxide + synthetic polypeptides	$C \sim 2.25$, $\rho \sim 1.1$, $\gamma = 40$, $\eta = 3.4$, $d = 125$, $Z = 21.3$	Electrode, EMI filter, $r \sim 120$	47
	N-Methyl-2-pyrrolidone/dimethyl sulfoxide/dimethylformamide/ethanol	$C = 0.8\text{--}12.5$, $\rho = 0.79\text{--}1.1$, $\gamma = 22.1\text{--}43.5$, $\eta = 7.3\text{--}13.8$, $d = 21$, $Z = 2.2\text{--}2.6$	Supercapacitors, $r \sim 50$	68
	Isopropanol	$C \sim 2$, $\rho = 0.8$, $\gamma = 23$, $\eta = 2.4$, $d = 22$, $Z \sim 8.3$	Broadband ultrafast laser generations, $r \sim 50$	This work

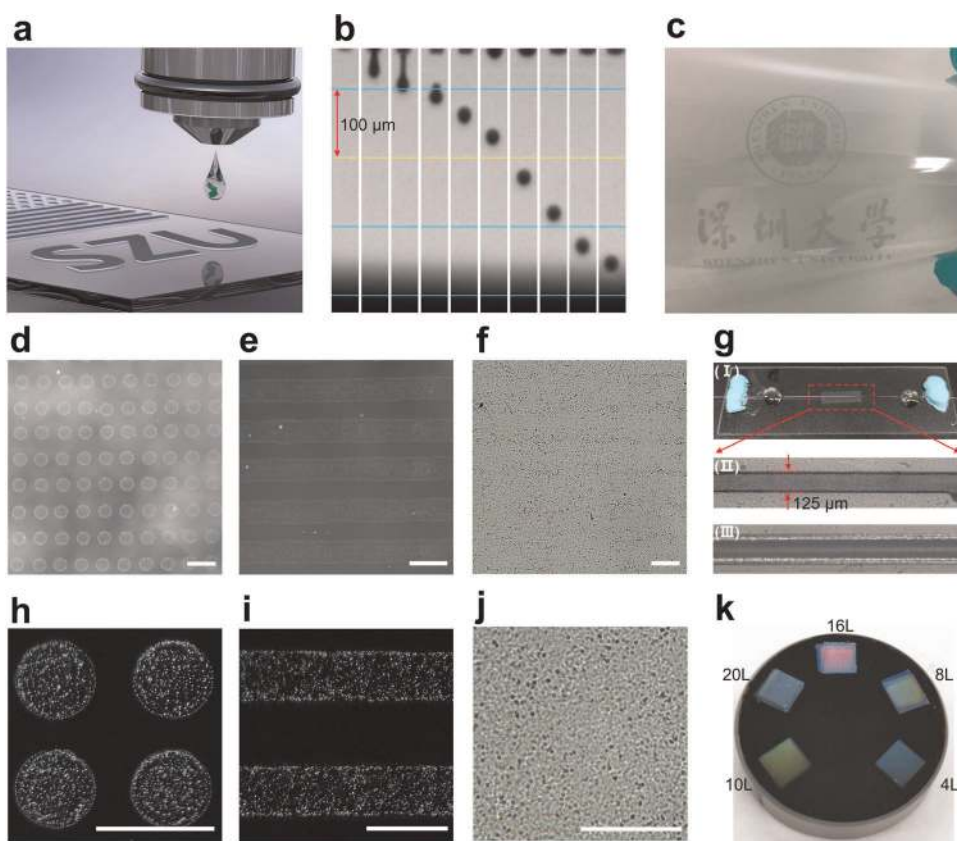


Fig. 2 Inkjet printing characterizations. **a** Inkjet printing schematic diagram. **b** Printing droplet sequences observed from the printer stroboscopic camera. **c** Inkjet printed logo of Shenzhen University on a transparent and flexible PET film. **d–f** and **h–j** The printed dots, stripes and plane on glass substrate, scale bar: 100 μm . **g** (I) The side-polished fiber saturable absorber. (II) Printed (12 layers) and (III) unprinted side-polished fiber checked by an optical microscope. **k** Inkjet printed MXene saturable absorber mirror (SAM) with different printing layers. The clockwise printed layers: 10 L, 20 L, 16 L, 8 L, 4 L

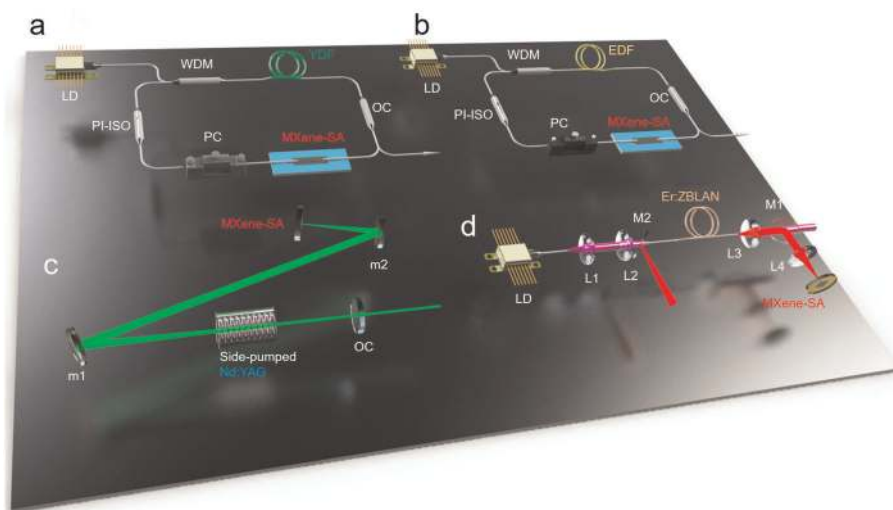


Fig. 3 Schematic diagrams of laser resonators. Laser diode pumped **a** Yb-doped and **b** Er-doped fiber laser resonators with an inkjet-printed MXene side-polished fiber saturable absorber. **c** Side-pumped Nd:YAG solid-state resonator, and **d** laser diode pumped Er-doped ZBLAN MIR fiber laser resonator with MXene printed on the end gold mirrors

The estimated intra-cavity net dispersion of Yb-doped and Er-doped are 0.227 ps² and −0.22 ps², respectively. The length of the side-polished portion is 10 mm, and the top surface has a close distance ($\sim 1 \mu\text{m}$) to the fiber guiding core to achieve efficient evanescent field-MXene interactions. In order to completely overlap the side-polished fiber, the rectangularly printing area is

$3 \times 12 \text{ mm}^2$. The MXene nanosheets are homogeneously printed on the side-polished fiber, as shown in Fig. 2g.

Compared to fiber resonator, all-solid-state resonator could be more challenge for free-space alignment and pulsed laser operation. Here, a side-pumped Nd:YAG solid-state laser resonator is conceived and constructed as shown in Fig. 3c. The size of Nd:

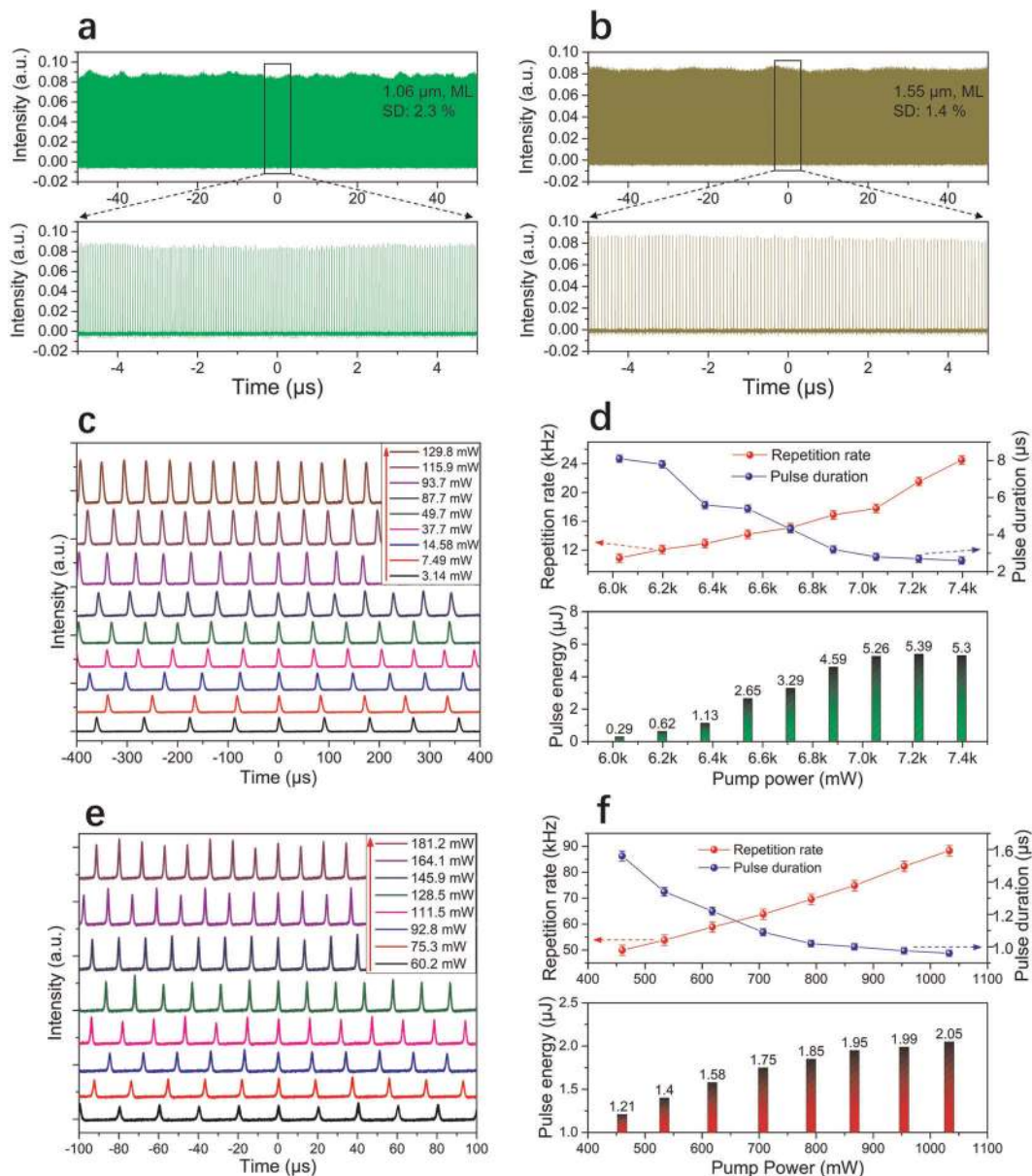


Fig. 4 Broadband pulsed laser operations. Oscilloscope spectrum of the phase locked pulse trains at **a** 1.06 μm and **b** 1.55 μm . The mode-locking pulse-to-pulse fluctuation is 2.3% and 1.4%, respectively. SD stand deviation. Pulse trains of Q-switched laser at **c** 1.06 μm and **e** 2.8 μm with the corresponding output powers. Q-switching pulse duration and repetition rate (up) and pulse energy (down) as a function of the pump power at **d** 1.06 μm and **f** 2.8 μm

YAG rod is $\Phi 3 \times 65$ mm. The side-pump source (GTPC-75S, GT Optics Co. Ltd) can deliver pump power as high as 75 W at the operation current of 25 A. Two concave mirrors with focal length of 250 mm (m1) and 50 mm (m2) are set up to achieve small beam profile on the printed MXene saturable absorber gold mirror. The output mirror has an output coupling efficiency of 20%. The absorber mirror is mounted on a manually transform xyz-stage to optimize the laser performance.

To further expand the laser operation regime of MXene, a linear fiber resonator incorporating the prepared MXene saturable absorber mirror is set up for mid-infrared ultrashort pulse generation, as shown in Fig. 3d. The pump source is supplied by a commercial laser diode (30 W, BTW Beijing Ltd) with wavelength center at 976 nm. The laser is coupled out with a fiber pigtail with a core diameter of 105 μm and numerical aperture (NA) of 0.15. The pump light is collimated by a biconvex lens ($f_1 = 50$ mm), then is focused into the gain fiber by the second biconvex lens ($f_2 =$

75 mm). The 3-meter double cladding Er:ZBLAN fiber (FiberLabs Inc.) was doped with an impurity concentration of 70,000 ppm. The core diameter of Er:ZBLAN fiber is 15 μm and NA of 0.12. The D-shape cladding has a diameter of 240×260 μm (short \times long) with NA of 0.4. To adjust the incident beam area thus the laser intensity on the MXene SAM and avoid the Fresnel refraction, a ZnSe aspherical lens pair ($f_3 = f_4 = 12.7$ mm, AR@976 nm, 2.7–3.7 μm) is established. A 45° dichroic mirror (M1) with high transparency at pump wavelength ($T > 95\%$) and high reflectivity at laser wavelength ($R > 99\%$) is added to remove the pump light effects on the MXene SA mirror. The outcoupling end facet of Er:ZBLAN fiber was cut perpendicular to the fiber axis, with a Fresnel reflection of 4% as the laser feedback. While the other facet was cut with a small angle of 8 degrees to avoid parasitic oscillation. Another identical 45° dichroic mirror (M2) was used to separate the pump and output light.

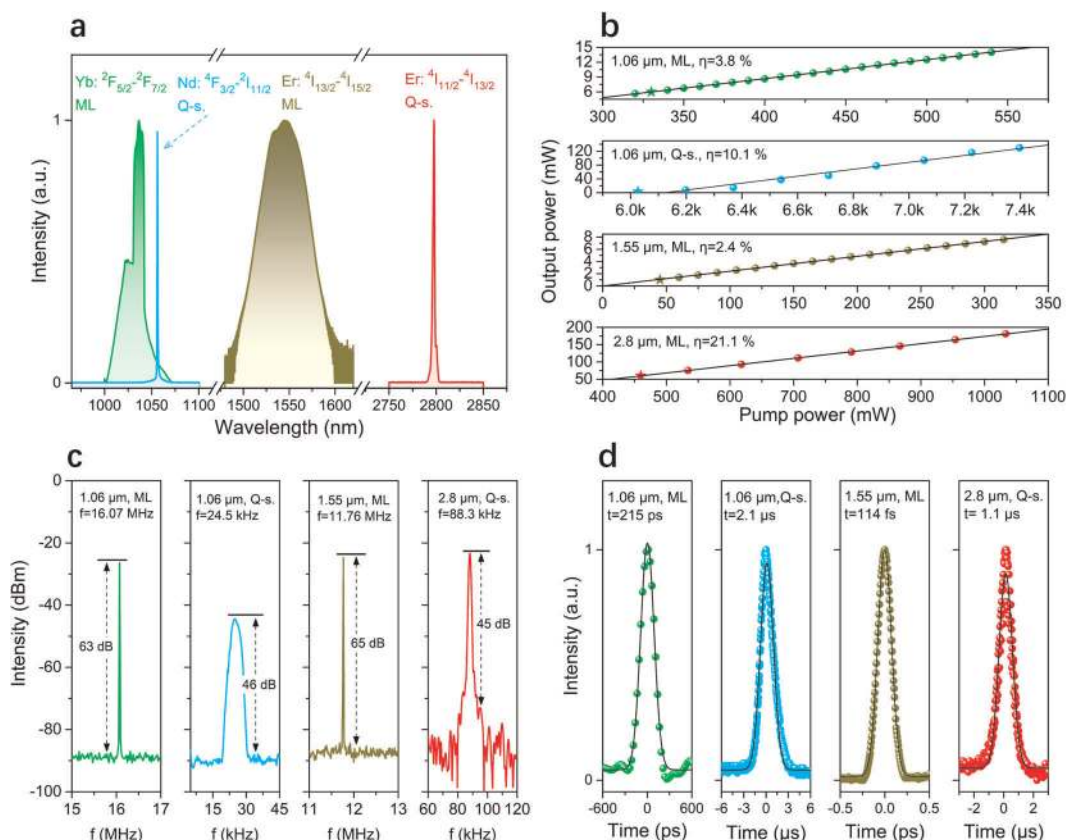


Fig. 5 Laser performance. **a** Laser operation wavelengths. The laser wavelength centers locate at 1034.5 nm (Yb: ${}^2F_{5/2}-{}^2F_{7/2}$), 1065.3 nm (Nd: ${}^4F_{3/2}-{}^4I_{11/2}$), 1543.5 nm (Er: ${}^4I_{13/2}-{}^4I_{15/2}$) and 2785.1 nm (Er: ${}^4I_{11/2}-{}^4I_{13/2}$), respectively. ML: mode-locking, Q-s.: Q-switching. **b** The output power and slope efficiency. The fitted laser thresholds are 176 mW, 6124 mW, 68.9 mW, and 178 mW, respectively. The stars indicate the pulsed laser operation thresholds. **c** Radio frequency spectrum of pulse laser operations. **d** The output laser pulse durations. Gaussian fit is applied. Time-bandwidth product (TBP) at 1.06 μm and 1.55 μm are estimated to be 391 and 0.367

Previous studies^{57,59} indicate that the nonlinear optical properties and linear losses of the saturable absorber can be finely tailored via directly varying the numbers of the printed layer. Here, fiber and gold mirror SAs with a range of printed layers are designed and fabricated. Stable continuous wave (CW) mode-locked (1.06 and 1.55 μm) and Q-switched (1.06 and 2.8 μm) lasers with the spectral ranges spanning from near- to mid-infrared regimes have been realized, as shown in Fig. 4. The mode-locked pulse trains show a low peak-to-peak fluctuation ($\sim 2\%$) over a time of 100 μs for the two operation wavelength, while the Q-switched pulse trains show a slightly higher fluctuation of ~ 5 and $\sim 6\%$ at 1.06 μm and 2.8 μm , respectively. The high stability of the pulsed laser operations is confirmed via the high signal-to-noise ratio (SNR) as shown in Fig. 5c. The repetition rate of phase-locking is a constant determined by the cavity length, to be 16.07 MHz and 11.76 MHz, respectively. However, the repetition rate of the Q-switching monotonically increases from 10.9 to 24.5 kHz at 1.06 μm , and 49.9 to 88.3 kHz at 2.8 μm . Conversely, the pulse duration decreases from 8.1 to 2.6 μs at 1.06 μm , and 1.56 to 1.1 μs at 2.8 μm in the meantime due to the increasing levels of saturation.

The laser wavelengths, output powers, repetition rates, and pulse durations of the laser operations in different resonators are summarized in Fig. 5. The steep spectral edges observed at the 1.06 μm (Yb: ${}^2F_{5/2}-{}^2F_{7/2}$) is because of the normal dispersion mode-locking operation. The wide frequency band (25.6 nm @3 dB) of Er: ${}^4I_{13/2}-{}^4I_{15/2}$ suggests the phase-locking can support an ultrashort temporal pulse (~ 114 fs) and is consistent with the autocorrelation characterization (APE pulseCheck 50), as shown in Fig. 5d (see more information in SI). As for the femtosecond laser

pulse, the fiber pigtail with non-negligible dispersion can significantly affect the output pulse duration.^{60,61} The fiber pigtail used here is a single-mode fiber with a length of $\sim 3\text{m}$, and an estimated dispersion of -0.065 ps². This indicates the output pulse experiences further compression during the output coupling. Different with the longitudinal mode phase-locked operation, the Q-switching operations show a relatively narrow spectrum band. A output slope efficiency as high as 21.1% (photonic efficiency of 60.5%) of the Q-switched mid-infrared operation was achieved. Noteworthy, all the pulsed laser operations can be initialized near the laser thresholds. The fundamental radio frequency is shown in Fig. 5c, high SNR radio frequency spectra can be observed from all the pulsed laser operations that confirms their high stability. The minimum pulse duration obtained at the highest pump level are 215 ps, 2.6 μs , 114 fs, and 1.1 μs , respectively. A comprehensive comparison of the laser performance with other reports using 2D materials-based saturable absorbers have been summarized in Tables S1–S4. Considering the maximum output power at the four wavelengths are 14.1 mW, 129.8 mW, 9.2 mW and 181.2 mW, respectively, the achieved maximum pulse energies (peak power) are 0.88 nJ (4.1 W), 5.3 μJ (2.1 W), 0.78 nJ (6.86 kW) and 2.1 μJ (1.9 W), which may suitable for a range of practical applications, e.g., mechanical machining,⁶² medical surgery,⁶³ ecological monitoring,⁶⁴ chemical reactions,⁶⁵ and spectroscopies.⁶⁶

We have described a full inkjet-printing approach for developing integrated broadband saturable absorbers via utilizing the distinct optical merits of 2D MXene. The well-controlled, cheap, binder-free and scalable ink formulation allows the agile integration of MXene small-footprint thin film patterns to variable setup geometrics. Ultrafast laser pulse generations were achieved

spanning from 1 μm to 3 μm with operations modes of CW phase-locking and Q-switching in both fiber and solid-state resonators. The obtained shortest pulse duration is going to 100 fs in the telecommunication window. Our demonstrates of versatile inkjet-printed MXene devices may pave the way to the realizations of advanced MXene photonics devices shortly. More spectacularly, we hope this work could offer inspirations to explore other full-print 2D crystals or heterostructures for integrated electro-photonics.

DATA AVAILABILITY

The data that support the findings of this study are available from the corresponding author upon reasonable request.

ACKNOWLEDGEMENTS

Financial support from the National Natural Science Foundation of China (Grant Nos. 61435010, 61575089, 61805146) and Science and Technology Innovation Commission of Shenzhen (Grant Nos. KQTD2015032416270385, JCYJ20150625103619275, JCYJ20170302153540973, and JCYJ20170412111625378), Science and Technology Planning Project of Guangdong Province (Grant No. 2016B050501005) and the Educational Commission of Guangdong Province (Grant No. 2016KCXTD006), Shenzhen-Hong Kong Innovation Cooperation Project (Grant No. SGLH20150205162842428), and the Science and Technology Development Fund (No. 007/2017/A1), Macao SAR, China are gratefully acknowledged.

AUTHOR CONTRIBUTIONS

H.Z. and X.J. conceived the project. X.J. and W.L. designed the experiments. X.J., W.L., T.H., and R.L. performed the experiments. Z.C. and C.L. instructed the inkjet printing experiments; Q.W. instructed the 1.06 μm and 1.55 μm fiber laser and 1.06 μm solid-state laser experiments; G.X. instructed the 2.8 μm MIR fiber laser experiments. All authors analyzed the data and discussed the experimental plans. X.J. wrote the manuscript and all authors commented and revised it. H.Z. supervised the whole project.

ADDITIONAL INFORMATION

Supplementary Information accompanies the paper on the *npj 2D Materials and Applications* website (<https://doi.org/10.1038/s41699-019-0117-3>).

Competing interests: The authors declare no competing interests.

Publisher's note: Springer Nature remains neutral with regard to jurisdictional claims in published maps and institutional affiliations.

REFERENCES

- Naguib, M. et al. Two-dimensional nanocrystals produced by exfoliation of Ti_3AlC_2 . *Adv. Mater.* **23**, 4248–4253 (2011).
- Anasori, B., Lukatskaya, M. R. & Gogotsi, Y. 2D metal carbides and nitrides (MXenes) for energy storage. *Nat. Rev. Mater.* **2**, 16098 (2017).
- Lin, H., Wang, X. G., Yu, L. D., Chen, Y. & Shi, J. L. Two-dimensional ultrathin MXene ceramic nanosheets for photothermal conversion. *Nano Lett.* **17**, 384–391 (2017).
- Xue, Q. et al. Photoluminescent Ti_3C_2 MXene quantum dots for multicolor cellular imaging. *Adv. Mater.* **29**, 6 (2017).
- Shahzad, F. et al. Electromagnetic interference shielding with 2D transition metal carbides (MXenes). *Science* **353**, 1137–1140 (2016).
- Ran, J. R. et al. Ti_3C_2 MXene co-catalyst on metal sulfide photo-absorbers for enhanced visible-light photocatalytic hydrogen production. *Nat. Commun.* **8**, 10 (2017).
- Li, R. Y., Zhang, L. B., Shi, L. & Wang, P. MXene Ti_3C_2 : an effective 2D light-to-heat conversion material. *ACS Nano* **11**, 3752–3759 (2017).
- Jiang, X. et al. Broadband nonlinear photonics in few-layer MXene $\text{Ti}_3\text{C}_2\text{T}_x$ ($T = \text{F}$, O , or OH). *Laser Photon. Rev.* **12** (2018).
- Zhang, X., Ma, Z. N., Zhao, X. D., Tang, Q. & Zhou, Z. Computational studies on structural and electronic properties of functionalized MXene monolayers and nanotubes. *J. Mater. Chem. A* **3**, 4960–4966 (2015).
- Xie, Y. & Kent, P. R. C. Hybrid density functional study of structural and electronic properties of functionalized $\text{Ti}_{n+1}\text{X}_n$ ($X = \text{C}$, N) monolayers. *Phys. Rev. B* **87**, 10 (2013).

- Lee, Y., Hwang, Y., Cho, S. B. & Chung, Y. C. Achieving a direct band gap in oxygen functionalized-monolayer scandium carbide by applying an electric field. *Phys. Chem. Chem. Phys.* **16**, 26273–26278 (2014).
- Balci, E., Akkus, U. O. & Berber, S. Band gap modification in doped MXene: Sc_2CF_2 . *J. Mater. Chem. C* **5**, 5956–5961 (2017).
- Dong, L., Kumar, H., Anasori, B., Gogotsi, Y. & Shenoy, V. B. Rational design of two-dimensional metallic and semiconducting spintronic materials based on ordered double-transition-metal MXenes. *J. Phys. Chem. Lett.* **8**, 422–428 (2017).
- Lee, Y., Cho, S. B. & Chung, Y. C. Tunable indirect to direct band gap transition of monolayer Sc_2CO_2 by the strain effect. *ACS Appl. Mater. Interfaces* **6**, 14724–14728 (2014).
- Hantanasirisakul, K. et al. Fabrication of $\text{Ti}_3\text{C}_2\text{T}_x$ MXene transparent thin films with tunable optoelectronic properties. *Adv. Electron. Mater.* **2**, 7 (2016).
- Ling, Z. et al. Flexible and conductive MXene films and nanocomposites with high capacitance. *Proc. Natl Acad. Sci. USA* **111**, 16676–16681 (2014).
- Nair, R. R. et al. Fine structure constant defines visual transparency of graphene. *Science* **320**, 1308–1308 (2008).
- Chaudhuri, K. et al. Highly broadband absorber using plasmonic titanium carbide (MXene). *ACS Photonics* **5**, 1115–1122 (2018).
- Jhon, Y. I. et al. Metallic MXene saturable absorber for femtosecond mode-locked lasers. *Adv. Mater.* **29** (2017).
- Sun, X. et al. Few-layer $\text{Ti}_3\text{C}_2\text{T}_x$ ($T = \text{O}$, OH , or F) saturable absorber for a femtosecond bulk laser. *Opt. Lett.* **43**, 3862–3865 (2018).
- Tuo, M. et al. Ultrathin 2D transition metal carbides for ultrafast pulsed fiber lasers. *ACS Photonics* **5**, 1808–1816 (2018).
- Gogotsi, Y. CHEMICAL VAPOUR DEPOSITION Transition metal carbides go 2D. *Nat. Mater.* **14**, 1079–1080 (2015).
- Dua, V. et al. All-organic vapor sensor using inkjet-printed reduced graphene oxide. *Angew. Chem. Int. Ed.* **49**, 2154–2157 (2010).
- Shin, K.-Y., Hong, J.-Y. & Jang, J. Micropatterning of graphene sheets by inkjet printing and its wideband dipole-antenna application. *Adv. Mater.* **23**, 2113–2118 (2011).
- Huang, L., Huang, Y., Liang, J., Wan, X. & Chen, Y. Graphene-based conducting inks for direct inkjet printing of flexible conductive patterns and their applications in electric circuits and chemical sensors. *Nano Res.* **4**, 675–684 (2011).
- Le, L. T., Ervin, M. H., Qiu, H., Fuchs, B. E. & Lee, W. Y. Graphene supercapacitor electrodes fabricated by inkjet printing and thermal reduction of graphene oxide. *Electrochem. Commun.* **13**, 355–358 (2011).
- Shin, K.-Y., Hong, J.-Y. & Jang, J. Flexible and transparent graphene films as acoustic actuator electrodes using inkjet printing. *Chem. Commun.* **47**, 8527–8529 (2011).
- Zhang, L. et al. Inkjet printing high-resolution, large-area graphene patterns by coffee-ring lithography. *Adv. Mater.* **24**, 436–440 (2012).
- Torresi, F. et al. Inkjet-printed graphene electronics. *ACS nano* **6**, 2992–3006 (2012).
- Li, J. et al. Efficient inkjet printing of graphene. *Adv. Mater.* **25**, 3985–3992 (2013).
- Withers, F. et al. Heterostructures produced from nanosheet-based inks. *Nano Lett.* **14**, 3987–3992 (2014).
- Secor, E. B., Prabhurashi, P. L., Puntambekar, K., Geier, M. L. & Hersam, M. C. Inkjet printing of high conductivity, flexible graphene patterns. *J. Phys. Chem. Lett.* **4**, 1347–1351 (2013).
- Secor, E. B., Ahn, B. Y., Gao, T. Z., Lewis, J. A. & Hersam, M. C. Rapid and versatile photonic annealing of graphene inks for flexible printed electronics. *Adv. Mater.* **27**, 6683–6688 (2015).
- Kim, J. et al. Direct exfoliation and dispersion of two-dimensional materials in pure water via temperature control. *Nat. Commun.* **6**, 8294 (2015).
- Santra, S. et al. CMOS integration of inkjet-printed graphene for humidity sensing. *Sci. Rep.* **5**, 17374 (2015).
- Dodoo-Arhin, D. et al. Inkjet-printed graphene electrodes for dye-sensitized solar cells. *Carbon* **105**, 33–41 (2016).
- Li, J. et al. Scalable fabrication and integration of graphene microsupercapacitors through full inkjet printing. *ACS nano* **11**, 8249–8256 (2017).
- Finn, D. J. et al. Inkjet deposition of liquid-exfoliated graphene and MoS_2 nanosheets for printed device applications. *J. Mater. Chem. C* **2**, 925–932 (2014).
- Kelly, A. G. et al. All-printed thin-film transistors from networks of liquid-exfoliated nanosheets. *Science* **356**, 69–73 (2017).
- Kelly, A. G., Finn, D., Harvey, A., Hallam, T. & Coleman, J. N. All-printed capacitors from graphene-BN-graphene nanosheet heterostructures. *Appl. Phys. Lett.* **109**, 023107 (2016).
- Carey, T. et al. Fully inkjet-printed two-dimensional material field-effect hetero-junctions for wearable and textile electronics. *Nat. Commun.* **8**, 1202 (2017).
- McManus, D. et al. Water-based and biocompatible 2D crystal inks for all-inkjet-printed heterostructures. *Nat. Nanotechnol.* **12**, 343–350 (2017).
- Li, J., Naiini, M. M., Vaziri, S., Lemme, M. C. & Östling, M. Inkjet printing of MoS_2 . *Adv. Funct. Mater.* **24**, 6524–6531 (2014).

44. Hu, G. et al. Black phosphorus ink formulation for inkjet printing of optoelectronics and photonics. *Nat. Commun.* **8** (2017).
45. Aleeva, Y. & Pignataro, B. Recent advances in upscalable wet methods and ink formulations for printed electronics. *J. Mater. Chem. C* **2**, 6436–6453 (2014).
46. Reis, N. & Derby, B. Inkjet deposition of ceramic suspensions: modeling and experiments of droplet formation. *MRS Online Proceedings Library Archive* **625** (2000).
47. Vural, M. et al. Inkjet printing of self-assembled 2D titanium carbide and protein electrodes for stimuli-responsive electromagnetic shielding. *Adv. Funct. Mater.* **28**, 1801972 (2018).
48. Shi, C. Y. et al. Structure of nanocrystalline Ti_3C_2 MXene using atomic pair distribution function. *Phys. Rev. Lett.* **112**, 5 (2014).
49. Van Osch, T. H., Perelaer, J., de Laat, A. W. & Schubert, U. S. Inkjet printing of narrow conductive tracks on untreated polymeric substrates. *Adv. Mater.* **20**, 343–345 (2008).
50. Derby, B. Inkjet printing of functional and structural materials: fluid property requirements, feature stability, and resolution. *Annu. Rev. Mater. Res.* **40**, 395–414 (2010).
51. Ying, Y. et al. Two-dimensional titanium carbide for efficiently reductive removal of highly toxic chromium(VI) from water. *ACS Appl. Mater. Interfaces* **7**, 1795–1803 (2015).
52. Shijian, L., Harris, T. & Wong, C. P. in *Proceedings International Symposium on Advanced Packaging Materials Processes, Properties and Interfaces (IEEE Cat. No.01TH8562)*. 299–304.
53. Papakonstantinou, D., Amanatides, E., Mataras, D., Ioannidis, V. & Nikolopoulos, P. Improved surface energy analysis for plasma treated PET films. *Plasma Process. Polym.* **4**, S1057–S1062 (2007).
54. Hu, H. & Larson, R. G. Marangoni effect reverses coffee-ring depositions. *J. Phys. Chem. B* **110**, 7090–7094 (2006).
55. Yin, Z., Huang, Y., Bu, N., Wang, X. & Xiong, Y. Inkjet printing for flexible electronics: materials, processes and equipments. *Chin. Sci. Bull.* **55**, 3383–3407 (2010).
56. Keller, U. et al. Semiconductor saturable absorber mirrors (SESAM's) for femto-second to nanosecond pulse generation in solid-state lasers. *IEEE J. Sel. Top. Quantum Electron.* **2**, 435–453 (1996).
57. Jiang, X. et al. Low-dimensional nanomaterial saturable absorbers for ultrashort-pulsed waveguide lasers. *Opt. Mater. Express* **8**, 3055–3071 (2018).
58. Jiang, X. et al. Epsilon-near-zero medium for optical switches in a monolithic waveguide chip at $1.9\ \mu\text{m}$. *Nanophotonics* **7**, 1835 (2018).
59. Jiang, X. et al. Bismuth telluride topological insulator nanosheet saturable absorbers for q-switched mode-locked Tm:ZBLAN waveguide lasers. *Ann. der Phys.* **528**, 543–550 (2016).
60. Tamura, K., Ippen, E. P., Haus, H. A. & Nelson, L. E. 77-fs pulse generation from a stretched-pulse mode-locked all-fiber ring laser. *Opt. Lett.* **18**, 1080–1082 (1993).
61. Haus, H. A., Tamura, K., Nelson, L. E. & Ippen, E. P. Stretched-pulse additive pulse mode-locking in fiber ring lasers: theory and experiment. *IEEE J. Quantum Electron.* **31**, 591–598 (1995).
62. Gattass, R. R. & Mazur, E. Femtosecond laser micromachining in transparent materials. *Nat. Photonics* **2**, 219–225 (2008).
63. Jean, B. & Bende, T. in *Solid-State Mid-Infrared Laser Sources Vol. 89 Topics in Applied Physics* (eds Irina T. Sorokina & Konstantin L. Vodopyanov) Ch. 12, 530–565 (Springer Berlin Heidelberg, 2003).
64. Vasil'ev, B. I. & Oussama, M. IR differential-absorption lidars for ecological monitoring of the environment. *Quantum Electron.* **36**, 801 (2006).
65. Zewail, A. H. Femtochemistry: atomic-scale dynamics of the chemical bond. *J. Phys. Chem. A* **104**, 5660–5694 (2000).
66. Popmintchev, T. et al. Bright coherent ultrahigh harmonics in the keV X-ray regime from mid-infrared femtosecond lasers. *Science* **336**, 1287–1291 (2012).
67. Kong, D., Le, L. T., Li, Y., Zunino, J. L. & Lee, W. Temperature-dependent electrical properties of graphene inkjet-printed on flexible materials. *Langmuir* **28**, 13467–13472 (2012).
68. Zhang, C. et al. Additive-free MXene inks and direct printing of micro-supercapacitors. *Nat. Commun.* **10**, 1795 (2019).



Open Access This article is licensed under a Creative Commons Attribution 4.0 International License, which permits use, sharing, adaptation, distribution and reproduction in any medium or format, as long as you give appropriate credit to the original author(s) and the source, provide a link to the Creative Commons license, and indicate if changes were made. The images or other third party material in this article are included in the article's Creative Commons license, unless indicated otherwise in a credit line to the material. If material is not included in the article's Creative Commons license and your intended use is not permitted by statutory regulation or exceeds the permitted use, you will need to obtain permission directly from the copyright holder. To view a copy of this license, visit <http://creativecommons.org/licenses/by/4.0/>.

© The Author(s) 2019